Nature Communications

https://doi.org/10.1038/s41467-026-70270-0

Article in Press

Reconstitution of woody biomass framework via dual-functional lignin engineering toward efficient and salt-resistant solar desalination

Received: 17 August 2025

Accepted: 23 February 2026

Cite this article as: Wang, B., He, Y., Yang, Z. *et al.* Reconstitution of woody biomass framework via dual-functional lignin engineering toward efficient and salt-resistant solar desalination. *Nat Commun* (2026). https://doi.org/10.1038/s41467-026-70270-0

Bin Wang, Yanrong He, Zhihao Yang, Qian Sun, Xipeng Zhang, Xiaojun Shen, Jia-Long Wen, Chaoji Chen & Tong-Qi Yuan

Reconstitution of Woody Biomass Framework via Dual-Functional Lignin Engineering Toward Efficient and Salt-Resistant Solar Desalination

Bin Wang [1,#], Yanrong He [1,#], Zhihao Yang [1,#], Qian Sun [1], Xipeng Zhang [1], Xiaojun Shen [1,], Jia-Long Wen [1], Chaoji Chen [2,*], Tong-Qi Yuan [1,*]*

[1] State Key Laboratory of Efficient Production of Forest Resources, Beijing Key Laboratory of Lignocellulosic Chemistry, Beijing Forestry University, Beijing 100083, China
[2] Hubei Biomass-Resource Chemistry and Environmental Biotechnology Key Laboratory, School of Resource and Environmental Sciences, Wuhan University, Wuhan 430079, China
[#] These authors contributed equally: Bin Wang, Yanrong He, and Zhihao Yang

E-mail: shenxiaojun@bjfu.edu.cn; chenchaojili@whu.edu.cn; ytq581234@bjfu.edu.cn

Abstract

Solar-driven interfacial evaporation is a promising solution to address global freshwater scarcity, with woody biomass-based evaporators standing out for their sustainability and cost-effectiveness. However, current woody biomass-based systems often suffer from inefficient water management and suboptimal photothermal performance. Herein, we develop a dual-function lignin-engineered reconstituted wood framework strategy, achieving both compositional and structural optimization of woody biomass to enhance its evaporation performance via water management and thermal management. By partially retaining and reconfiguring lignin within the woody biomass framework, a higher fraction of loosely bound "intermediate water" with reduced evaporation enthalpy is generated while preserving the water-pumping capability. Concurrently, the extracted lignin is upcycled via laser-induced graphitization into a broadband photothermal layer composed of hierarchical graphene/graphitic carbon structures with solar absorptivity exceeding 95%. This synergistic design results in the E-150 solar evaporator, which achieves an evaporation rate of 2.24 $kg\,m^{-2}\,h^{-1}$ and a photothermal conversion efficiency of 91.52% under one-sun irradiation, surpassing most reported wood-based evaporators. Moreover, the retained lignin sustains multiscale channel integrity, imparting strong salt resistance, high recyclability, and robust purification capabilities. This integrated biomass valorization strategy provides a scalable, low-cost, and eco-friendly route for high-performance solar desalination and sustainable water-energy applications.

Introduction

The escalating global water crisis, driven by population growth, industrialization and climate change, has rendered freshwater increasingly scarce[1]. Seawater, which makes up nearly 97.5% of the Earth's water resources, is a viable source, particularly for coastal regions facing severe freshwater shortages, but conventional desalination methods (reverse osmosis or multistage flash) are energy-intensive and costly[2,3]. In contrast, interfacial solar evaporation offers a promising alternative, which harnesses highly renewable solar energy to heat only a thin surface layer of water, minimizing thermal losses and operational complexity[4]. This approach can transform seawater and wastewater into drinkable water in a low-cost, eco-friendly manner, which is critical for coastal and arid regions facing chronic freshwater shortages. Interfacial solar evaporation typically consists of a photothermal top layer that absorbs sunlight and an underlying wick or porous matrix that transports water upward[5, 6]. Wood, being an abundant and renewable natural product, possesses a layered porous structure with low-curvature channels capable of floating on water[7,8]. Combined with anisotropic thermal conduction across cross-section and longitudinal sections, wood holds significant potential for application in interfacial solar evaporation[9].

State-of-the-art materials have pushed photothermal conversion toward the thermodynamic limit, so further gains depend on improved water management[10]. Studies have demonstrated that structural or chemical tuning can induce a higher fraction of intermediate water with fewer hydrogen bonds in certain synthetic 3D polymeric materials[11,12], whose evaporation efficiency is up to 86 times that of free water. Such regulation markedly reduces the evaporation enthalpy of water within the material and accelerates the evaporation rate. It should be noted that the term “evaporation enthalpy” used herein does not refer to the strict thermodynamic definition, but rather to a generalized concept denoting the overall energy required for liquid water confined within the material to transition into vapor. However, native wood contains hydrophobic lignin that tightly binds cellulose fibers together, which tends to impede the pumping of water to the evaporation interface. Many reported wood evaporators therefore chemically remove lignin from wood to open its pores and increase wettability[13-15]. For example, Gu et al. demonstrated a fully wood-based

evaporator using completely delignified wood, achieving an efficiency of 91.74% efficiency and a 1.93 kg m^{-2} h^{-1} evaporation rate[16]. However, complete removal of lignin has drawbacks, and it entirely consumes the lignin resource and, importantly, eliminates the only intrinsic hydrophobic component of wood. As a result, excessive hydrophilicity leads to domination by high-enthalpy water (combined water and free water), and limits the ultimate evaporation rate[17]. Recent molecular simulations and experiments confirm that introducing an appropriate amount of hydrophobic components can help create more intermediate water with low evaporation enthalpy by weakening the hydrogen bond network between the matrix and water[18]. Therefore, as the only hydrophobic component and binder in wood, the controlled presence of lignin can actually be leveraged to water states inside wood from both spatial and chemical composition perspectives. Adjusting the lignin content in wood to maintain effective water pumping capacity while increasing the intermediate moisture content paves the way for high-performance woody biomass-based solar evaporators with better economic and environmental benefits, making them more suitable for large-scale application than hydrogel solar evaporators.

Another challenge in woody biomass-based evaporators is achieving efficient photothermal conversion while maintaining sustainability. Natural wood is weakly absorptive of sunlight, so most designs deposit external coatings (e.g., plasma metal nanoparticles or semiconductor inks) to boost absorption[19-21]. These additives can add cost and environmental risk, conflicting with the goal of green desalination. Carbon-based nanomaterials, especially graphene, have been widely used in the photothermal conversion system of woody biomass-based solar evaporators due to their broad-spectrum absorption, high photothermal conversion efficiency, strong stability, and high abundance[22,23]. Notably, lignin, with its aromatic ring structure and high carbon content[24], can promote the formation of sp^2 hybrid ordered structure of graphene crystals, making it an ideal raw material for preparing graphene[25,26]. However, cumbersome processes and harsh preparation conditions limit the large-scale development of lignin-based graphene. Laser etching technology, with the advantages of simple operation, low cost, high precision, energy saving and environmental protection[27], can ignore the severe heterogeneity of lignin, promoting the sustainable development

of lignin-based photothermal conversion materials[28].

In this work, we developed a lignin-engineered reconstituted woody framework strategy that simultaneously addresses two key challenges in solar evaporation based on sustainability and economy, and the efficient preparation of high-performance photothermal layers and the reduction of water evaporation enthalpy (Fig. 1). We hypothesize that appropriate lignin removal modulates both the spatial microstructure and the distribution of functional groups, promoting the formation of intermediate water with weaker hydrogen bonding. This lowers the evaporation enthalpy while preserving effective water transport to the evaporation interface. Simultaneously, the removed lignin is not wasted, which is recovered and processed via laser etching into a composite carbon layer composed of graphite carbon and graphene. This lignin-engineered reconstitution wood not only outperforms most reported woody biomass-based solar evaporators in terms of evaporator performance but also has significant environmental and economic benefits, which holds great promise for promoting the large-scale application of woody biomass-based solar evaporators.

Results

Water states within the lignin-engineered reconstituted wood

As shown in Fig. S1 and Table S1, the lignin content decreased from 25.77% in natural wood (labelled as Wood) to 16.70% in W-150 obtained after pretreatment with an alcohol solution system at 150 °C. In contrast, the lignin in W-A, obtained by sodium chlorite delignification, was almost completely removed. The hydrophilicity of the woody biomass framework significantly affects water pumping capacity and water states[16]. The hydrophilicity of W-150 improved due to partial removal of the hydrophobic lignin, while W-A, lacking lignin, exhibited better hydrophilicity (Fig. S2). The increase in the hydrophilicity of the woody biomass framework facilitates the water pumping to the evaporation interface. However, previous reports have shown that excessive hydrophilicity will lead to the dominance of free water, which has a high evaporation enthalpy (about 86 times the enthalpy of intermediate water), thereby limiting the further evaporation rate[29-31]. The influence of lignin content on the water states within the woody biomass framework stems from two perspectives (Fig. 2a). Firstly, lignin, as a main component of lignocellulose, is entangled

with cellulose and hemicellulose[32-34]. Therefore, lignin content closely affects the crosslinking degree of the woody biomass framework. On the other hand, lignin contains both hydrophilic functional groups (such as phenolic and aliphatic hydroxyl), as well as hydrophobic phenyl ring structures (the only hydrophobic component in lignocellulose). That affects the formation of hydrogen bonds between the woody biomass framework and water molecules in a moist state, thus impacting the number and strength of those hydrogen bonds. In addition, pretreatment selectively enriched syringyl (S) units in lignin of W-150 (L-W150), elevating the S/G ratio from 2.31 in lignin of Wood (L-Wood) to 5.05 in L-W150 (Figs. 2b and S3). Concurrently, the pretreatment process induces cleavage of lignin ether bonds (primarily β-*O*-4 linkages), and promotes condensation reactions that result in the formation of more hydrophobic C–C bonds (Fig. S4). These collective changes in the lignin structure may make it easier for water to evaporate from the substrate[35-38].

To test these hypotheses, differential scanning calorimetry (DSC), dark evaporation experiments, Raman and low field nuclear magnetic resonance (LF-NMR) were systematically employed to investigate the effect of lignin on the water states and the evaporation enthalpy of water in woody biomass frameworks. As shown in Fig. S5a, the DSC curve of pure water showed a sharp peak. The water peak in W-A flattened out, but still had sharp peaks, indicating too much free water. In W-150, the water appeared broader and lacked sharp peaks. The evaporation enthalpies of water in pure W-A and W-150 calculated from the DSC curve were 1990 and 1670 J/g, respectively (Fig. S5b). In the dark evaporation experiment, as shown in Fig. 2c, the evaporation enthalpies of water in W-A and W-150 were 1842 and 1397 J/g, respectively. The results of both methods showed that proper lignin content was beneficial in reducing the evaporation enthalpy of water.

To further explore the effect of lignin content on the evaporation enthalpy of water in the wood, woody biomass frameworks with different lignin content were obtained under the pretreatment condition of 140-170 ºC. The evaporation enthalpy of water in the woody biomass framework obtained by DSC increased with the decrease in lignin content, and W-140 had the

lowest evaporation enthalpy (Fig. S5b). However, the evaporation enthalpy of water obtained by the dark evaporation experiment decreased first and then increased with the decrease of lignin content, and W-150 had the lowest evaporation enthalpy (Fig. S5c). This discrepancy arises because DSC measurements account not only for the evaporation of intermediate water and free water, but also for the most tightly bound water, whereas the dark evaporation experiment primarily involves the evaporation of intermediate water and free water. As a result, the evaporation enthalpy determined by DSC is typically higher than that obtained by the dark evaporation experiment, particularly for highly hydrophilic substrates. W-150, with lower lignin content, had better hydrophilicity and more bound water than W-140, resulting in a higher evaporation enthalpy obtained by DSC. It is worth noting that the actual use of solar evaporators almost does not involve the evaporation of bound water, which is closer to the dark evaporation experiment[39]. Therefore, the results of the dark evaporation experiment were used as the basis for the subsequent discussion.

LF-NMR was used to investigate spin proton relaxation, providing information on the nuclear mobility of bound and free water[23]. The transversal relaxation properties of water in the woody biomass framework were investigated by 1D LF-NMR, which attempted to explain the influence mechanism of lignin content on water states in wood. Generally, the water that is more tightly bound to the wood (such as bound water) has a shorter transverse relaxation time (T_2); conversely, the free water has a longer T_2[23]. As shown in Fig. S6a, the T_2 distribution curve of Wood showed four peaks, indicating the presence of four water states. Relaxation peaks of T_2 less than 1 ms (T_{21}) and around 1000 ms (T_{24}) are attributed to bound and free water, respectively[40,41]. Large amounts of capillary water were present in fine channels in the wood, which appeared at the T_{23} relaxation peak near 45 ms[42], while acromion (T_{23}) might be intermediate water in the large diameter channels. It was found that the content of bound and free water in W-A increased, but the T_{22} peak belonging to intermediate water disappeared (Fig. 2d), indicating that the absence of lignin was not conducive to the formation of intermediate water. As for W-150, the T_{22} and T_{23} peaks were combined, showing that the properties of capillary water at this time were very similar to those of intermediate

water. However, capillary water is difficult to distinguish between bound water and intermediate water through 1D LF-NMR.

To further subdivide capillary water, 2D LF-NMR was used to characterize the water states in the woody biomass framework, which effectively reduces the interference caused by water overlap and chemical composition. The longitudinal relaxation time (T_1) can reflect the time for the nuclei of high-energy states to return to the ground state through energy exchange with the surrounding environment during relaxation, while T_2 corresponds to the time it takes for a high-energy nucleus to transfer energy to a similar low-energy nucleus and return to the ground state[43]. The T_1/T_2 value indicates the mobility of hydrogen atoms, and a lower value means that the water molecule is more mobile. As shown in Fig. S6b, four main peaks could be observed in the 2D LF-NMR spectrum of Wood, among which the D peak with the largest T_1/T_2 value is usually identified as the signal of polymers or bound water in wood, while the A peak with the smallest T_1/T_2 value represents free water. Peaks B and C originated from capillary water, which corresponded to the water in the amorphous region of microfibrils and its surrounding hemicellulose, as well as the water in the amorphous region of the hemicellulose and lignin, respectively[44]. Since lignin and hemicellulose were almost completely removed, no peak C appeared in the 2D LF-NMR spectrum of W-A, and a strong peak A was observed (Fig. 2e). The stronger peak A and the weaker peak B indicated that capillary water in W-A had similar properties to free water. Notably, a strong peak B was observed in the 2D LF-NMR spectrum of W-150, which were further divided into peaks B_1 and B_2 to distinguish better the capillary water states (Fig. 2f). The peak B_2 with a smaller T_1/T_2 value had better water mobility, indicating that water molecules were clustered under the action of hydrogen bonds, which was not conducive to water evaporation. The water in peak B1 was judged as intermediate water. Compared with W-A and Wood, the B_1 signal in W-150 was significantly enhanced, which meant that W-150 had more intermediate water. Moreover, to be closer to the actual use scenario, 2D LF-NMR tests were performed on W-A and Wood in a water-filled state. As shown in Fig. S7, only one strong peak was shown in both spectra. By comparison, W-150 had a larger T_1/T_2 value than W-A, which once again verified that W-150 had a larger intermediate

water content.

To prove the existence of different water forms, Raman spectroscopy of various woody biomass frameworks was fitted into four peaks by the Gaussian function, as shown in Fig. S8. The results showed that W-150 presented the largest ratio of intermediate water to free water due to the proper delignification, consistent with the analysis of evaporation enthalpy and LF-NMR. Moreover, note that since a certain amount of lignin was still retained as a support, the multistage channels in W-150 were intact, especially the ray cells (Fig. S9), which will facilitate the transverse shuttle of salt ions, protecting the salt resistance[45]. In summary, the hydrophilicity, functional group composition and crosslinking degree of the woody biomass framework were affected by lignin content. Appropriate lignin retention encouraged the production of more intermediate water in the woody biomass framework (especially in the capillary region), which could effectively pump water to the evaporation interface while reducing the evaporation enthalpy, thereby increasing the evaporation rate. In addition, due to the partial retention of lignin, the multistage channel structure was preserved intact, which was conducive to salt resistance.

Laser-etched surfaces

The lignin recovered during the ethanol solution pretreatment was coated on the surface of W-150, which was then laser etched to prepare the photothermal conversion layer of the evaporator (Fig. 3a). After laser etching, the surface of the evaporator shows increased hydrophilicity (Figs. 3b and S10) and an orderly porous structure (Fig. 3c). As shown in Fig. 3e, compared with other carbonization technologies, the graphitized layer obtained by laser etching technology showed a satisfying surface morphology (rich, multi-layered and ordered hierarchical pores) and a specific surface area of up to 100.77 m^2 g^{-1}(Fig. S11). The micronscale macropores facilitate effective capture of incident sunlight, while the mesopores and micropores efficiently absorb scattered and reflected light. This hierarchically ordered porous architecture induces a pronounced blackbody effect, significantly enhancing broadband solar absorption and localized photothermal conversion. Moreover, the high specific surface area of the porous carbon layer promotes the formation of nano/microscale water droplets with a lower evaporation enthalpy on the surface, which will be

proved in subsequent experiments. Furthermore, regardless of the coating process or the laser etching process, the multistage channels and transversely shuttling ray cells in the woody biomass framework were retained (Fig. S12), which would guarantee the anti-salt crystallization performance of E-150. Furthermore, the laser etching depth of close to 60 μm (Fig. 3d) and the laser-induced graphene (LIG) observed inside the large channels within the woody biomass framework (Fig. S13) would further promote sunlight absorption.

In addition to the orderly porous structure, the LIG had a crystal region with a lattice spacing of 0.349 nm (Fig. 3e), which could be attributed to the spacing of the two adjacent (002) planes in graphitic carbon[46]. Moreover, as shown in Fig. 3f, three main peaks could be observed in the Raman spectrum of the E-150 surface. Among them, the D-peak (1340 cm^{-1}) and G-peak (1570 cm^{-1}) are attributed to lattice defects (sp^3 hybridization) of carbon atoms and in-plane stretching vibrations of sp^2 hybridization of carbon atoms, respectively[47,48]. The peak (2670 cm^{-1}) comes from second-order band-boundary phonons, which are usually related to the number of graphene layers[49]. The distinct peak and small I_D/I_G value (0.69) indicated the presence of graphene with fewer stacked layers. However, there was still some sp^3 hybridization at the edges of the surface carbon layer. The results of the TEM and Raman analyses showed that both graphene and graphitic carbon were present in the surface carbon layer. Graphene can effectively absorb sunlight from the ultraviolet to infrared range and has high photothermal conversion efficiency and thermal conductivity[50]. However, the complex preparation process and the exorbitant price of graphene make it impractical to use the photothermal conversion layer composed only of graphene. Moreover, graphene usually requires support material to enhance its structural stability and mechanical strength, but the interface compatibility with the support material still faces difficulties[51]. In LIG, porous graphitic carbon served as a support material for graphene, which not only provided a high specific surface area to promote the absorption of sunlight, but also complements the disadvantages of graphene without having to consider interface compatibility issues to overcome the defects of limited light absorption efficiency and single light absorption direction of few-layer graphene monomers. Observing the changes of elements after laser etching

showed that carbon elements increased and oxygen elements decreased significantly (Fig. S14). Combined with the previous reports, the graphitization mechanism could be inferred. Due to the violent vibration within lignin molecules caused by laser radiation, the local temperature rapidly increased, resulting in C-O bond and C=O bond breaking and gas release (Fig. 3a) [52-54]. At the same time, a part of the region underwent a transition from sp^3 hybridization state to sp^2 hybridization state, and the benzene ring structure of lignin was organized into a graphene structure. It was worth noting that untreated balsa wood had little carbonization effect on the surface of the wood substrate at the same laser power due to the lack of sufficient lignin on its surface (Fig. S15).

The ability of the evaporator's photothermal conversion layer to absorb sunlight was enhanced (Fig. S16). As shown in Fig. S17, compared with W-150, the light absorption capacity of C-150 in the short-wavelength band was increased due to the introduction of lignin, but there was almost no change in the long-wavelength band. Under the synergistic action of graphene and graphitic carbon, the light absorption capacity of E-150 in the full band of 300-2500 nm had been significantly improved, exhibiting an absorption rate of up to 95.48% for sunlight, which was much higher than that of the W-150 and C-150 (Fig. 3g). The LIG (a composite material composed of graphene and porous graphitic carbon) obtained by laser etching of lignin showed high sunlight absorption capacity and potentially competitive photothermal conversion efficiency. Furthermore, A simple process of this work is advantageous for the large-scale preparation of a reconstituted wood solar evaporator. According to the experimental conditions of this work, we further scaled up the production, achieving a large-sized evaporator of 0.88 m^2 or an evaporator of arbitrary shape to meet the requirements of complex practical conditions (Figs. 3h and S18).

Evaporation properties

Based on the above analysis, partial delignification significantly enhanced the intermediate water content. Moreover, LIG derived from recovered lignin on the surface of the evaporator demonstrated high solar absorption and photothermal conversion efficiency. These characteristics established a solid foundation for the development of high-performance woody biomass-based solar evaporators. As shown in Fig. 4a, woody biomass-based solar evaporators E-W, E-A and E-

150 were prepared based on Wood, E-A and E-150, respectively, and evaporation rates were 1.51, 1.72 and 2.24 kg m^{-2} h^{-1} under one sunlight, respectively. Since the manufacturing process of the photothermal conversion layer was the same, the difference in evaporation rates was mainly due to the woody biomass framework. According to the analysis results in Section 2.1, the woody biomass framework of E-W contained a large amount of lignin, resulting in its insufficient ability to pump water to the evaporation interface, while the water within E-A was dominated by free water with high enthalpy of evaporation due to its better hydrophilicity. In the case of E-150, appropriate delignification increased the intermediate water content in the woody biomass framework while efficiently pumping water to the evaporation interface. Moreover, the photothermal conversion layer composed of graphite carbon and graphene not only had strong light absorption capacity and photothermal conversion efficiency, but also promoted the formation of microdroplets with low evaporation enthalpy in the pumped water (Fig. S19), thus improving the evaporation performance. In addition, the comparison of woody biomass-based solar evaporators with different lignin content showed that the evaporation rate first increased and then decreased with the decrease of lignin content, and E-150 showed the highest evaporation rate (Fig. 4b), which corresponded to the analysis results of intermediate water content.

Based on W-150, the influence of laser power on the evaporation performance was also discussed. As shown in Figs. 4c and S20, when the laser power was less than 45%, lignin could not be effectively graphitized, resulting in low light absorption performance and photothermal conversion efficiency of the evaporator surface. However, when the laser power was excessive (50%), Raman spectra showed a large I_D/I_G value and almost no 2D peaks could be observed (Fig. S21). At this time, the surface of the evaporator was over-graphitized, mainly composed of graphite carbon, and almost no graphene structure. Therefore, achieving a composite carbon layer with the complementary advantages of graphite carbon and graphene was impossible, reducing light absorption and photothermal conversion capacity. Furthermore, the photothermal conversion capability of the evaporator was investigated by measuring the temperature change of the surface. Fig. 4g showed that the temperature of the evaporator surface rapidly rose to 39.1 °C in 1 min

under one solar irradiation, indicating the strong photothermal conversion capability of the E-150. After 30 min of irradiation, the temperature of the evaporator surface was stable at about 50 ºC, and the water temperature was 31 ºC, indicating a thermal localization effect, mainly due to the low thermal conductivity caused by the porous structure of the wood. The thermal localization effect could reduce the heat loss during evaporation and improve the evaporation performance.[55,56]

Due to water and thermal management, the E-150 exhibited an evaporation rate of up to 2.24 kg m^{-2} h^{-1} and a photothermal conversion efficiency of 91.52% under one solar irradiation (Fig. 4d), surpassing most reported woody biomass-based solar evaporators (Fig. 4e and Table S3). Although a few reported woody biomass-based solar evaporators have evaporation performance close to or better than the E-150, these preparation processes are complex and require the introduction of metals or metal oxides, which further increases their cost and potential environmental hazards. Furthermore, the introduction of carbon dots can endow the evaporator with evaporation performance comparable to that of E-150, but the preparation of these carbon dots requires a large amount of reagents and a long processing time (over 20 hours), resulting in a low efficiency of evaporator preparation. Different from these advanced woody biomass-based solar evaporators mentioned above, this work uses fully biomass-based materials, with a low energy consumption, short processing time, and no additional metal materials to prepare highly efficient woody biomass-based solar evaporators. Fabricating the evaporator solely from lignocellulosic components (wood and lignin) enhances sustainability and scalability, aligning with the eco-friendly approach of recent all-wood evaporators. Compared to reported woody biomass-based solar evaporators similar or better evaporation performance, it demonstrated environmental and economic benefits (Fig. 4f). This highlights its exceptional potential for commercial application, underscoring its promising scalability and market viability in sustainable technology solutions.

Seawater desalination and wastewater purification

Salt ions in seawater/sewage will concentrate, crystallize and accumulate during evaporation, resulting in salt pollution[57]. As shown in Fig. 5a, the evaporation rate of E-150 in simulated brine

with 3.5% and 5.0% salinity stabilized at about 2.15 kg m^{-2} h^{-1} within 6 h under one solar irradiation, which was almost the same as that in pure water. In addition, when the brine salinity was increased to 10%, the evaporation rate was reduced to 1.96 kg m^{-2} h^{-1}, but the performance remained stable during the long evaporation process (Fig. S22). However, when the salinity exceeded 20%, salt crystallization occurred at the evaporation interface of E-150, causing the evaporation rate to continue decreasing. These results showed that E-150 had an acceptable resistance to salt crystallization, which was suitable for all seawaters in the world, and some high-salinity brines from industry (≤10%). The salt resistance of E-150 was mainly due to the partial retention of lignin in the woody biomass framework, which made the interconnected multistage channel structure intact. As shown in Fig. 5b, these multistage channels provided low-tortuosity pathways with different hydraulic conductivities. When the desalination was carried out, the water flux in the small-diameter channel was smaller than that in the large-diameter channel, resulting in a larger salt concentration in the small-diameter channel. The resulting in-plane concentration gradient encouraged salt ions to shuttle transversally through the ray cell. Simultaneously, salt ions accumulated inside the large-diameter channels diffused back into the seawater. This multidirectional mass transfer characteristic not only endowed E-150 with anti-salt crystallization properties, but also enabled the salt crystals on the evaporator surface to be efficiently eliminated under dark conditions (Fig. S23). The efficient elimination of salt crystals under dark conditions could further broaden the practical application scenarios of E-150 through the day-night cycle.

To verify the application of E-150 under the actual sun (Fig. 5c), an outdoor evaporation test was conducted in actual seawater from the Bohai Sea (approximately 40° N and 121° E) on September 19, 2024 in Beijing, China (8:00-17:00). During the evaporation test, the water vapor is condensed in the cooling area to avoid the effect of light occlusion and light refraction by the condensation water at the top (Fig. S24). As shown in Fig. 5d, the evaporation rate of E-150 gradually increased in the initial stage, and stabilized at about 2.00 kg m^{-2} h^{-1} from 11:00 to 14:00, demonstrating the practical application potential of E-150. It is worth noting that the lower evaporation rate in practical applications is due to the weaker solar flux in Beijing during autumn.

The long-term stability and cycling performance of E-150 were investigated using actual seawater. As shown in Fig. 5e, E-150 was continuously evaporated in seawater for 12 h under one solar irradiation, showing a stable evaporation rate of 2.16 kg m^{-2} h^{-1}, and almost no salt crystallization was observed. Moreover, during 10 consecutive 4 h evaporation tests, the evaporation rate of E-150 still remained stable (Fig. 5g), demonstrating long-term stability. Furthermore, the E-A and E-150 used in seawater were air-dried at room temperature, and their recyclability was compared. As shown in Figs. 5f and S25, there was almost no change in E-150 after recovery, while the volume of E-A was sharply reduced after recovery, and the surface carbon layer was seriously damaged. The recyclability of E-150 was attributed to the rigidity provided by the partially retained lignin (Fig. S26). In contrast, E-A lacking lignin not only could not be recycled, but also was prone to surface collapse during the process of lignin solution coating (Fig. S27). Furthermore, due to the higher proportion of intermediate water with weak hydrogen-bonding characteristics in E-150, the binding energy between this water and contaminant particles is smaller. Thus, E-150 exhibits enhanced purification capacity (Fig. S28).

Discussion

This work demonstrates a compositional and structural reconstitution strategy of a woody biomass framework that enables simultaneous optimization of water transport and photothermal conversion in solar evaporators. We reveal that partially retained lignin facilitates the formation of intermediate water, thereby reducing the evaporation enthalpy while ensuring effective water pumping to the evaporation interface. Simultaneously, the photothermal conversion layer prepared by laser etching of lignin combined the advantages of graphene and graphite carbon while exhibiting an ordered multistage pore structure, which had strong light absorption capacity, photothermal conversion efficiency and promoted the formation of microdroplets with low enthalpy of evaporation. Under one-sun illumination, the evaporator E-150 achieves a high evaporation rate of 2.24 kg m^{-2} h^{-1} and a photothermal conversion efficiency of 91.52%, outperforming most previously reported woody biomass-based solar evaporators. Additionally, the appropriate lignin content in the woody biomass framework provided a solid guarantee for the

evaporator's anti-salt crystallization performance, recovery, and purification performance. Overall, our results confirm this hypothesis. The lignin-engineered wood evaporator indeed achieves significantly higher evaporation rate and enhanced salt resistance, demonstrating that the proposed dual-functional strategy successfully optimizes both water management and photothermal conversion for solar desalination. The reconstituted woody framework strategy proposed in this work offers a simple, low-energy, and cost-effective method with substantial potential for large-scale application, providing a promising model for the sustainable development of woody biomass-based solar evaporators, balancing both economic and environmental benefits.

Methods

Materials The chemical composition of balsa wood from Fujian Province, China, is shown in Table S1, and the size of the sample used in this study was 10*10*5 mm. Aluminum chloride hexahydrate (97.0%), sodium hypochlorite pentahydrate (≥39%), sodium alginate (AR), sodium hydroxide (96%), ethanol (99.7%), methylene blue (≥70.0%), and direct red 80 (≥25%) were purchased from Aladdin Co., Ltd. Other reagents were analytical grade and purchased from Macklin Co., Ltd. The actual seawater was taken from China's Bohai Sea (approximately 40° N and 121° E) in October 2023, which was not further treated before use.

Pretreatment in alcohol solution system Before pretreatment, the balsa wood blocks were immersed in a reaction mixture, ethanol-water solution (1:1), with 0.02 mol/L aluminum chloride for 2 days. The soaked balsa wood blocks and the reaction mixture were added into a polytetrafluoroethylene-lined reactor for delignification pretreatment for 3 h, and the effect of pretreatment temperature (140-170 °C) was studied in detail. After the pretreatment, the wood blocks were taken out and immersed in a 50% ethanol aqueous solution to replace the solution containing lignin, and this step was repeated twice. Finally, the wood blocks were immersed in deionized water to displace the ethanol and freeze-dried to obtain a woody biomass framework (W-140 to W-170). For the pretreatment liquid, ethanol was recovered by vacuum rotary evaporation, and lignin was obtained by centrifuging for subsequent laser etching. It was worth noting that all chemicals used in this section were easily recyclable.

In addition, as a control sample, wood was completely lignin-removed by the traditional sodium chlorite process to obtain woody biomass framework W-A, and the lignin in this process could not be recovered. Specific operations were described in the Supplementary Information.

Laser etching To better contrast, the lignin used for laser etching was the lignin recovered from the above pretreatment temperature of 160 ºC. 0.5 g lignin as the carbon source and 0.2 g sodium alginate as the binder were dissolved in 10 mL of 0.1 M sodium hydroxide solution, then 0.3 mL solution was evenly coated on the surface of a woody biomass framework and air-dried. Subsequently, 0.3 mL of the solution was evenly coated on the surface of the woody biomass framework and air-dried. Finally, a series of woody biomass-based solar evaporators were obtained by laser etching using a semiconductor laser engraving machine with a peak laser power of 7.0 W, and a laser wavelength of 450 nm. Except for the samples that investigated the effect of laser power, the laser power used in the etching process of the other samples was 45%, and the scanning rate was 70 mm/s.

Material Characterization After the woody biomass framework was crushed, its chemical composition was determined using the previously reported method[58], and see the Supplementary Information for details. The morphologies and energy-dispersed X-ray spectroscopy (EDS) were observed by scanning electron microscope (SEM, Hitachi Regulus8100, Japan) and high-resolution transmission electron microscopy (HRTEM, JEM-2100, Japan). Raman spectra of graphitization layers and water in woody biomass frameworks were detected by Raman microscopy (X-plor, France). Surface wettability was determined by an OCA20 Contact angle measurement system (Data-physics, Germany). The light absorption capacity of the evaporator was recorded by UV–visible-NIR spectrophotometer (UV3600, Shimadzu, Japan). The evaporation enthalpies of water in the woody biomass framework were determined by a differential scanning calorimeter (DSC-60 Plus, Shimadzu, Japan) and a dark evaporation experiment, respectively. The compressive strength of wood was measured by a universal testing machine (UTM6530, China). The type of water in the woody biomass framework was characterized by low-field nuclear magnetic resonance (1D/2D LFNMR, VTM20-010V-I, China).

Solar Evaporation Experiment A 300 W xenon lamp (PLS-SXE3000, China) with an AM 1.5G filter was used to simulate sunlight, and a densitometer (CELNP2000-2(10)A, China) was used to adjust the radiation intensity at the evaporation interface to one sunlight (about 1 kW m^{-2}). The surface temperature of the woody biomass-based evaporator and water temperature were recorded with an infrared thermal imager (FLIR-E4, USA). Mass changes during evaporation were measured using an electronic balance (BSM-220.4, China) with an accuracy of 0.0001 g. The evaporation rate (v) was calculated in equation (1) as follows:

$$v=\Delta m/s*\Delta t \quad (1)$$

Where Δm was the overall mass change, s was the area at the top of the evaporator, and Δt was the irradiation time change.

The photothermal conversion efficiency (η) of the evaporator was calculated by equation (2) as follows:

$$\eta=v*H_E/(C_{opt}*P_i) \quad (2)$$

Where v was the evaporation rate at a steady state, H_E was the evaporation enthalpy of water in the corresponding sample, C_{opt} was the light absorption coefficient of the evaporator surface as shown in Fig. 3g, and P_i was the radiant power of one sun (1 kW m^{-2}).

In addition, the water vapour generated by the evaporator was collected by a self-made device (Figs. 5c and S24) to measure the purification capacity of the evaporator. An inductively coupled plasma source mass spectrometer (ICP-MS, Agilent 7800ce, USA) was used to measure the concentration of metal ions in water, while the concentration of dyes in water was measured by an ultraviolet spectrophotometer (UV-2450, Japan).

Data availability

All data needed to evaluate the conclusions in the paper are present in the paper, the Supplementary Information, or from the corresponding author upon request. Source Data are provided with this paper.

References

1. Shannon MA, et al. Science and technology for water purification in the coming decades. *Nature.* **452**, 301-310 (2008).
2. Kim Y, Lee W-g. Seawater and its resources. In: *seawater batteries: principles, materials and technology*). Singapore: Springer Nature Singapore (2022).
3. Chaule S, et al. Rational design of a high performance and robust solar evaporator via 3D-printing technology. *Adv. Mater.* **33**, 2102649 (2021).
4. Chen C, Kuang Y, Hu L. Challenges and opportunities for solar evaporation. *Joule.* **3**, 683-718 (2019).
5. Tao P, et al. Solar-driven interfacial evaporation. *Nat. Energy.* **3**, 1031-1041 (2018).
6. Wu X, et al. Interfacial solar evaporation: from fundamental research to applications. *Adv. Mater.*, 2313090 (2024).
7. He S, et al. Nature-inspired salt resistant bimodal porous solar evaporator for efficient and stable water desalination. *Energy Environ. Sci.* **12**, 1558-1567 (2019).
8. Chen L, et al. 3D-printed tripodal porous wood-mimetic cellulosic composite evaporator for salt-free water desalination. *Compos. Part. B-Eng.* **263**, 110830 (2023).
9. Chao W, et al. Enhanced wood-derived photothermal evaporation system by in-situ incorporated lignin carbon quantum dots. *Chem. Eng. J.* **405**, 126703 (2021).
10. Xu N, Song Y, Wei T, Zhu J. Flatband λ-Ti_3O_5 boosts solar evaporation. *Joule.* **7**, 2665-2667 (2023).
11. Li L, et al. Polyelectrolyte ydrogel-functionalized photothermal sponge enables simultaneously continuous solar desalination and electricity generation without salt accumulation. *Adv. Mater.*, 2401171 (2024).
12. Zhao F, et al. Highly efficient solar vapour generation via hierarchically nanostructured gels. *Nat. Nanotechnol.* **13**, 489-495 (2018).
13. Ma X, et al. Wood-based solar-driven interfacial evaporators: design and application. *Chem. Eng. J.*, 144517 (2023).
14. Chen L, et al. Biomass waste-assisted micro (nano) plastics capture, utilization, and storage for sustainable water remediation. *The Innovation.* **5**, 100655 (2024).
15. Qin Q, et al. “Bottom-up” and “top-down” strategies toward strong cellulose-based materials. *Chem. Soc. Rev.* **53**, 9306-9341 (2024).
16. Gu Y, et al. Solar-powered high-performance lignin-wood evaporator for solar steam generation. *Adv. Funct. Mater.* **33**, 2306947 (2023).
17. Petridis L, Smith JC. Molecular-level driving forces in lignocellulosic biomass deconstruction for bioenergy. *Nat. Rev. Chem.* **2**, 382-389 (2018).
18. Thybring E, Fredriksson M, Zelinka S, Glass S. Water in wood: a review of current understanding and knowledge gaps. *Forests.* **13**, (2022).
19. Dong Y, et al. Reviewing wood-based solar-driven interfacial evaporators for desalination. *Water Res.* **223**, 119011 (2022).
20. Gnanasekaran A, Rajaram K. Flake-like CuO nanostructure coated on flame treated eucalyptus wood evaporator for efficient solar steam generation at outdoor conditions. *Colloid. Surface. A.* **662**, 130975 (2023).
21. Gu Y, et al. All wood-based evaporator via cell wall regulating for integrated water and energy generation. *Adv. Funct. Mater.*, e19230 (2025).
22. Wu W, et al. Cellulose-based Interfacial solar evaporators: structural regulation and performance

manipulation. *Adv. Funct. Mater.* **33**, 2302351 (2023).

23. Li XP, et al. Reshapable MXene/graphene oxide/polyaniline plastic hybrids with patternable surfaces for highly efficient solar-driven water purification. *Adv. Funct. Mater.* **32**, 2110636 (2022).
24. Wang B, et al. Harnessing renewable lignocellulosic potential for sustainable wastewater purification. *Research.* **7**, 0347 (2024).
25. Tran CD, et al. Sustainable energy-storage materials from lignin–graphene nanocomposite-derived porous carbon film. *Energy Technology.* **5**, 1927-1935 (2017).
26. Okamoto S, et al. Additive effect of graphene and lignin-derived graphene on radical polymerization behaviors of methacrylate monomers. *Macromol. Chem. Phys.* **224**, 2300276 (2023).
27. Lin J, et al. Laser-induced porous graphene films from commercial polymers. *Nat. Commun.* **5**, 5714 (2014).
28. Yang Z, et al. One-step sustainable preparation of laser induced S-doped graphene for assembly of high-performance Naturesupercapacitors. *J. Clean. Prod.* **450**, 141956 (2024).
29. Zhao F, et al. Materials for solar-powered water evaporation. *Nat. Rev. Mater.* **5**, 388-401 (2020).
30. Wei D, et al. Water activation in solar-powered vapor generation. *Adv. Mater.* **35**, 2212100 (2023).
31. Gnanasekaran A, Rajaram K. Rational design of different interfacial evaporators for solar steam generation: Recent development, fabrication, challenges and applications. *Renew. Sust. Energ. Rev.* **192**, 114202 (2024).
32. Zhang C, et al. Unveiling the structural characteristics of lignin and lignin–carbohydrate complexes in fibers and parenchyma cells of moso bamboo during different growing years. *J. Agric. Food. Chem.* **72**, 20537-20546 (2024).
33. Tarasov D, Leitch M, Fatehi P. Lignin–carbohydrate complexes: properties, applications, analyses, and methods of extraction: a review. *Biotechnol. Biofuels.* **11**, 269 (2018).
34. Yang Z, et al. One-pot lignocellulose fractionation towards efficient whole sugar conversion and aromatic monomer production using a mild alkaline oxidation system. *Green. Chem.* **27**, 6244-6259 (2025).
35. Wang J, Qian Y, Li L, Qiu X. Atomic force microscopy and molecular dynamics simulations for study of lignin solution self-assembly mechanisms in organic–aqueous solvent mixtures. *ChemSusChem.* **13**, 4420-4427 (2020).
36. Bregado JL, Secchi AR, Tavares FW. A density functional theory study on interactions in water-bridged dimeric complexes of lignin. *Phys. Chem. Chem. Phys.* **26**, 9234-9252 (2024).
37. Hackenstrass K, Hasani M, Wohlert M. Structure, flexibility and hydration properties of lignin dimers studied with Molecular Dynamics simulations. *Holzforschung.* **78**, 98-108 (2024).
38. Cesari L, Canabady-Rochelle L, Mutelet F. Computational study of phenolic compounds-water clusters. *Struct. Chem.* **29**, 625-643 (2018).
39. Xuemin G, Peng Y, Yanfen W. How to reduce enthalpy in the interfacial solar water generation system for enhancing efficiency? *Nano Energy.* 109434 (2024).
40. Jing S, et al. The critical roles of water in the processing, structure, and properties of nanocellulose. *ACS nano.* **17**, 22196-22226 (2023).
41. Jia L, et al. Crystal Nonlinearity. *Nano Letters.* **24**, 1753-1760 (2024).
42. Engelund ET, Thygesen LG, Svensson S, Hill CA. A critical discussion of the physics of wood–water interactions. *Wood. Sci. Technol.* **47**, 141-161 (2013).
43. Bonnet M, et al. NMR determination of sorption isotherms in earlywood and latewood of Douglas fir. Identification of bound water components related to their local environment. *Holzforschung.* **71**, 481-490

(2017).

44. Li J, Ma E. Characterization of water in wood by time-domain nuclear magnetic resonance spectroscopy (TD-NMR): a review. *Forests.* **12**, 886 (2021).
45. Kuang Y, et al. A high-performance self-regenerating solar evaporator for continuous water desalination. *Adv. Mater.* **31**, 1900498 (2019).
46. Zhang W, et al. Lignin laser lithography: a direct-write method for fabricating 3D graphene electrodes for microsupercapacitors. *Adv. Energy Mater.* **8**, 1801840 (2018).
47. Zhang C, et al. An integrated and robust plant pulse monitoring system based on biomimetic wearable sensor. *npj Flexible Electronics.* **6**, 43 (2022).
48. Shen F, et al. A closed-loop strategy for ciprofloxacin adsorption and degradation by acetic acid/H_2O_2 modified biochar. *Chin. J. Chem. Eng.* **89**, 314-323 (2025).
49. Wu J-B, et al. Raman spectroscopy of graphene-based materials and its applications in related devices. *Chem. Soc. Rev.* **47**, 1822-1873 (2018).
50. Xie Z, et al. The rise of 2D photothermal materials beyond graphene for clean water production. *Adv. Sci.* **7**, 1902236 (2020).
51. Mohan VB, Lau K-t, Hui D, Bhattacharyya D. Graphene-based materials and their composites: A review on production, applications and product limitations. *Compos. Part. B-Eng.* **142**, 200-220 (2018).
52. Zhang H, et al. Probing laser-induced structural transformation of lignin into few-layer graphene. *Green. Chem.* **26**, 5921-5932 (2024).
53. Le TSD, et al. Ultrafast laser pulses enable one-step graphene patterning on woods and leaves for green electronics. *Adv. Funct. Mater.* **29**, 1902771 (2019).
54. Chyan Y, et al. Laser-induced graphene by multiple lasing: toward electronics on cloth, paper, and food. *ACS Nano.* **12**, 2176–2183 (2018).
55. Pang B, et al. Molecular-scale design of cellulose-based functional materials for flexible electronic devices. *Adv. Electron. Mater.* **7**, 2000944 (2021).
56. Du C, et al. Heat-localized solar evaporation: transport processes and applications. *Nano Energy.* **107**, 108086 (2023).
57. Lin X, et al. Fully lignocellulosic biomass-based double-layered porous hydrogel for efficient solar steam generation. *Adv. Funct. Mater.* **32**, 2209262 (2022).
58. Sluiter A, et al. Determination of structural carbohydrates and lignin in biomass. *Laboratory analytical procedure.* **1617**, 1-16 (2008).

Acknowledgements

This work was supported by the National Natural Science Foundation of China (22308029) (X. S.), the Knowledge Innovation Program of Wuhan-Basi Research (2023020201010072) (C. C.), the Fundamental Research Funds for the Central Universities (691000003) (C. C.), and the 5·5 Engineering Research & Innovation Team Project of Beijing Forestry University (No. BLRC 2023B05) (T. Y.). Additionally, the authors appreciate the assistance of the Innovation Platform for

High-Value Utilization of Forest Resources at Beijing Forestry University. We thank Insight Vision for their professional assistance in creating the three-dimensional rendering for Figure 1.

Author contributions

T.Y., C.C., X.S. and B.W. conceived the concept, processing, and structure details. B.W., Y.H. and Z.Y. performed the design and preparation of the evaporator. B.W. and Y.H. carried out the evaporation test. B.W., Y.H., and Z.Y. co-wrote the manuscript. T.Y., C.C. and X.S. supervised the work and revised the manuscript. J.W. provided guidance on the structural analysis of lignocellulose. Q.S. provided assistance in the enthalpy of the evaporation test of water. X.Z. participated in large-scale sample preparation and outdoor evaporation tests. All authors commented on the submitted version of the manuscript.

Competing interests

The authors declare no competing interests.

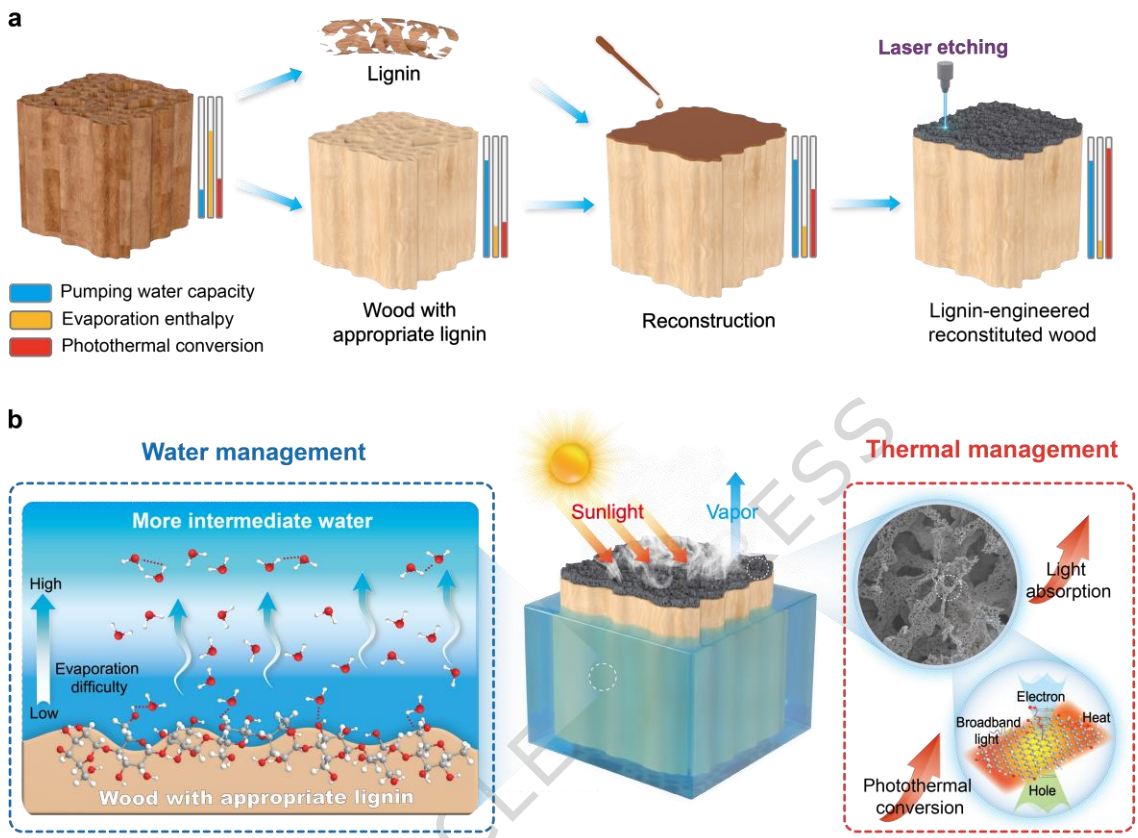

Fig. 1. Schematic diagram of the preparation and internal mechanism of the woody biomass-based solar evaporator. a Schematic diagram of lignin-engineered reconstituted woody framework strategy. **b** The dual functions of lignin within woody biomass-based solar evaporators in water management and thermal management. The three-dimensional elements were professionally rendered by Insight Vision based on our conceptual input.

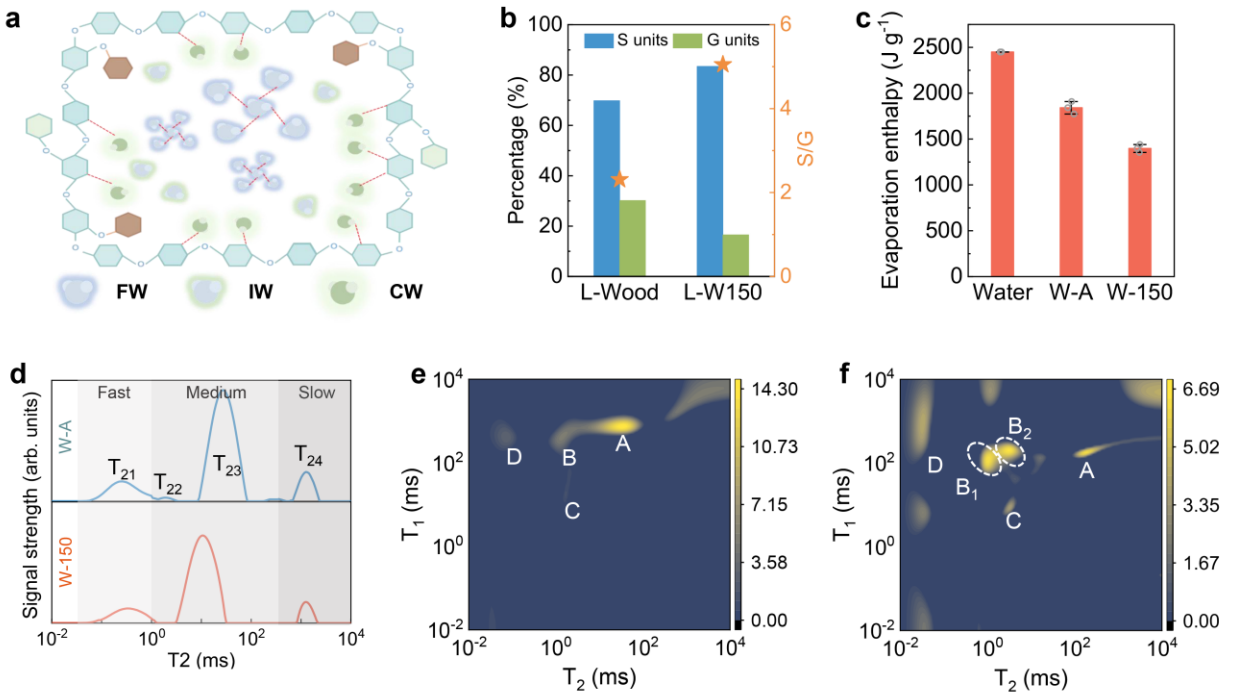

Fig. 2. Water management for wood with an appropriate amount of lignin. a Schematic diagram of the interaction between water and molecular chains in W-150 and the water states. Cellulose (blue hexagons), hemicellulose (green pentagons), and lignin (brown hexagons) are symbolically shown to illustrate their structural roles. **b** The proportion of the structural unit calculated based on the quantitative 2D-HSQC NMR spectra (400 MHz, DMSO-d_6)**. c** Evaporation enthalpy of water in W-A and W-150 measured by the dark evaporation experiment. Values in **c** represent their means ± SDs (standard deviation) from n = 3 independent samples. Source data are provided as a Source Data file. **d** The T_2 distribution of W-A and W-150 in the fiber saturated state. T_1-T_2 correlation spectra of **e**) W-A, and **f**) W-150 in the fiber saturated state.

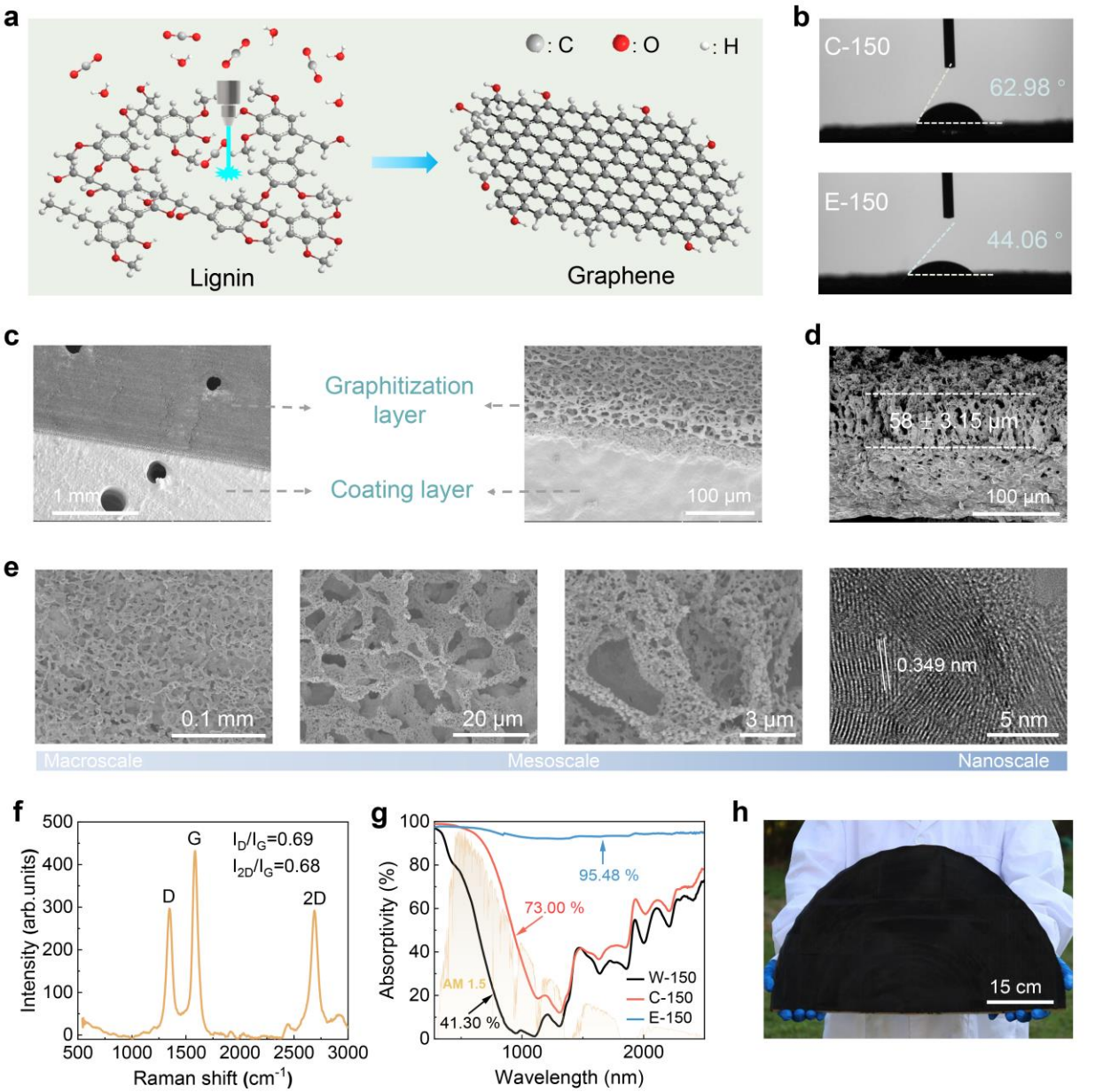

Fig. 3. Characterization of the structure and light absorption performance of the top layer. **a** Schematic diagram of graphene preparation by laser etching of lignin. **b** Surface wettability of C-150 and E-150. C-150 was the W-150 coated with lignin solution; E-150 represented the woody biomass-based solar evaporator obtained by laser etching of the C-150. **c** SEM comparison images before and after laser etching. **d** SEM image of a cross-section of the E-150 surface. **e** SEM and HR-TEM images of the E-150 surface at different scales. **f** Raman spectra of the E-150 photothermal conversion layer. **g** Solar absorptivity of woody biomass-based solar evaporators and the normalized spectral solar irradiance density of air mass 1.5 global (AM 1.5 G) tilt solar spectrum. **h** Large laser-etched woody biomass-based solar evaporator.

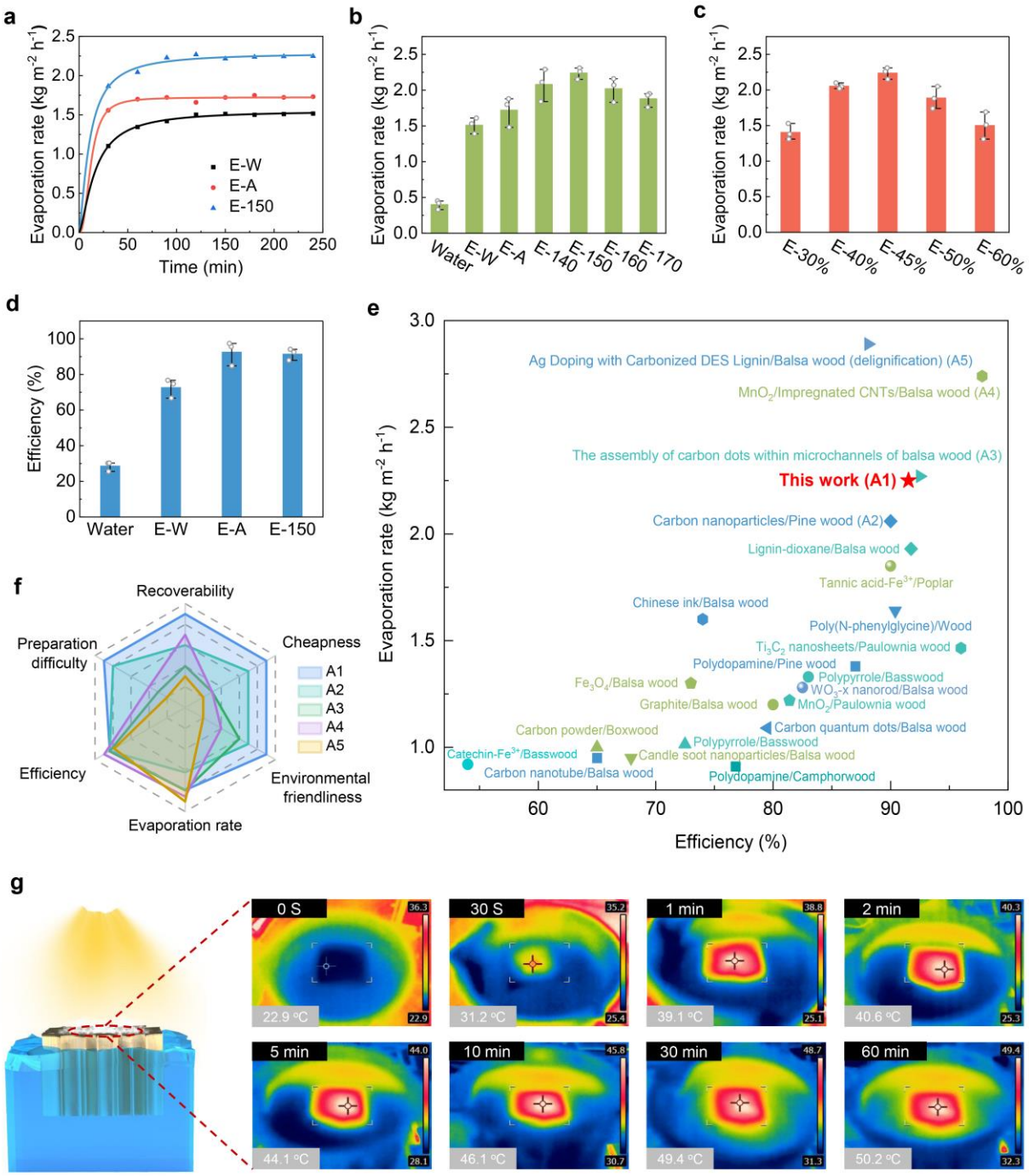

Fig. 4. The evaporation performance of lignin-engineered recombinant wood. a Evaporation rate curves of E-W, E-A and E-150 under one solar irradiation. **b** Stable evaporation rates of woody biomass-based solar evaporators with different lignin content under one solar irradiation (All evaporators were prepared based on W-150, with the X in E-X representing laser power, n = 3). **c** Effect of laser power on the evaporation rate of the woody biomass-based solar evaporator (n = 3). **d** Photothermal conversion efficiencies of E-W, E-A and E-150 under one solar irradiation (n = 3). **e** Comparison with previously reported woody biomass-based solar evaporators in terms of

evaporation rate and photothermal conversion efficiency under one solar irradiation, and the detailed data are shown in Table S3. **f** A comprehensive comparison with previously reported woody biomass-based solar evaporators. **g** The infrared thermal images of the E-150 surface temperature with time. Values in b, c and d represent their means ± SDs (standard deviation) from n = 3 independent samples. Source data are provided as a Source Data file.

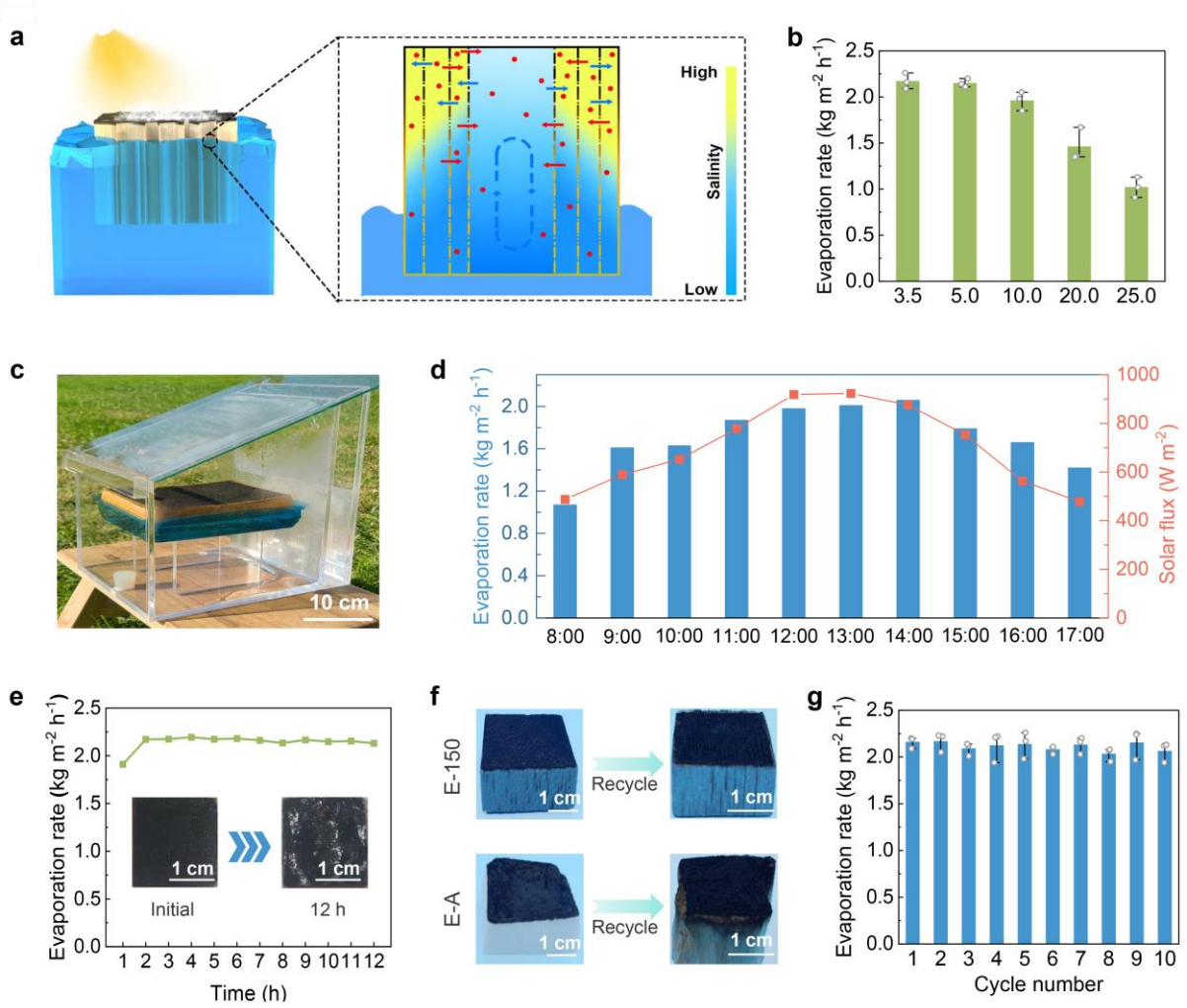

Fig. 5. Multifunctional performance of lignin-engineered reconstituted wood: salt resistance, recyclability, and purification. a Evaporation rate of E-150 in brines with different salinities under one solar radiation. **b** Schematic diagram for resistance to salt crystallization of E-150. **c** The outdoor water evaporation experiment of E150 (n = 3). **d** Synchronous solar flux, and evaporation rates of E-150 from 8:00 to 17:00 in the outdoor experiment (Temperature range: 20-29 °C, Humidity range: 50%-60%, Solar radiation intensity as shown in Fig. 5d, Beijing, China, September 19, 2024). **e** The change in evaporation rate of E-150 in real seawater after continuous evaporation for 12 h under one solar radiation, and the salt crystallization after continuous evaporation for 12 h as shown in the illustration. **f** Images of the E-A and E-150 before and after recycling. **g** Average evaporation rate of E-150 in real seawater for 10 consecutive 4 h under one solar radiation (n = 3). Values in b, and g represent their means ± SDs (standard deviation) from n = 3 independent samples. Source data are provided as a Source Data file.

Editorial summary: Biomass-based systems for solar evaporation are a promising sustainable method to address global freshwater scarcity; however current systems are inefficient. Here the authors report a dual-function lignin-engineered reconstituted wood framework for a biomass-based solar evaporator.

Peer review information: *Nature Communications* thanks the anonymous reviewers for their contribution to the peer review of this work. A peer review file is available.